Progress In Electromagnetics Research C, Vol. 90, 109–124, 2019

Spherical Mapping of the Second-Order Phoenix Cell for Unbounded Direct Reflectarray Copolar Optimization

Vincent Richard[1], Renaud Loison[1, *], Raphael Gillard[1], Herve Legay[2], Maxime Romier[3], Jean-Paul Martinaud[4], Daniele Bresciani[2], and Fabien Delepaux[2]

Abstract—A general synthesis approach is proposed for reflectarrays using second order Phoenix cells. It relies on an original spherical representation that transforms the optimization domain in a continuous and unbounded space with reduced dimension. This makes the synthesis problem simpler and automatically guarantees smooth variations in the optimized layout. The proposed mapping is combined with an Artificial Neural Network (ANN) based behavioral model of the cell and integrated in a min/max optimization process. Bi-cubic spline expansions are used to decrease the number of variables. As an application, a contoured beam for space communication in the [3.6–4.2] GHz band is considered. The gain improvement compared to an initial Phase Only synthesis (POS) is up to 1.62 dB at the upper frequency. Full-wave simulation of the final array is provided as a validation.

1. INTRODUCTION

Passive ReflectArrays (RA) are promising antennas for applications requiring high gain, low profile, and low mass [1]. Preliminary demonstrations have been published for directive beams [2], contoured beams [3–6] or for dual-polarization [7, 8]. Most of them rely on a quite simple design process where only the phase of the main polarization at one frequency is controlled over the radiating aperture (Phase Only Synthesis, POS). Typically, this is done by selecting the geometry of each elementary cell on the reflecting panel so that it provides the desired local phase. Generally, the tuning of a single geometrical parameter is sufficient to obtain an almost 360° phase range and, then, a simple one-to-one correspondence between cell geometry and local phase can be established.

However, more advanced synthesis approaches [9, 10] are needed when specifications get more stringent, as for dual and multiple frequency RA or large bandwidth contoured beams for space communications. In this case, RA could advantageously compete with shaped reflectors whose fabrication is both complex and expensive. Nevertheless, their design has to address several simultaneous goals, directly at the radiation pattern level. The cell selection process is then the result of a complex trade-off. Naturally, stringent specifications also require more complex cells, with several independent geometrical parameters, in order to be able to meet the different goals. This contributes further to increased complexity. Indeed, required advanced synthesis approaches have to handle multiple goals for the array radiation by tuning multiple degrees of freedom (DoF) at each cell. For a realistic RA made of several thousands of cells, this really becomes a challenging task. On the other hand, it is believed that the successful management of this task is a key point in RA design since the availability of so many DoF may offer unique opportunity to outperform classical reflectors.

Received 23 October 2018, Accepted 10 February 2019, Scheduled 27 February 2019

* Corresponding author: Renaud Loison (Renaud.Loison@insa-rennes.fr).

[1] Institute of Electronics and Telecommunications of Rennes (IETR), UMR CNRS 6164, INSA, CS 70839, Rennes 35708, France. [2] Thales Alenia Space, Toulouse 31037, France. [3] Centre National des Etudes Spatiales (CNES), Toulouse 31400, France. [4] Thales Defense Mission Systems (DMS), Elancourt 78990, France.

At this stage, a deeper insight in RA design approaches is necessary to better understand the associated challenges. As full-wave EM optimization of RA is not possible yet, design approaches usually involve a 2-step process. The first step aims at providing a full characterization of the chosen cell, by computing its complete reflection matrix [11] for any set of geometrical parameters. To do so, full-wave simulations are carried out, considering a single cell in a periodic environment (local-periodicity assumption). The resulting data is then used all along the optimization process and a very rapid access mechanism is thus essential. Most approaches rely on lookup tables with appropriate interpolating schemes [6]. Equivalent circuits can also be used [12]. Combined with filter synthesis techniques [13], they have demonstrated good capabilities for FSS [14] and even RA synthesis [15], especially regarding bandwidth optimization. Unfortunately, they are usually restricted to canonical geometries and normal incidence. Behavioral models based on Artificial Neural Networks (ANN) are more general [16, 17]. They have been used in [18] to tune the geometry of each RA cell of a narrow band RA. Here, in continuation to [19] and [20], we use 2 different ANN, one for magnitude and one for phase, in order to improve the prediction accuracy of the full reflection matrix. Efficient approaches based on ordinary kriging and support vector machines have also been proposed recently [21]. Whatever the used model, the second step in the design approach is to select the best geometry for all cells, in order to meet the specifications for the array radiation. Theoretically, this requires an iterative process in which all degrees of freedom are varied and the radiation pattern of the array is re-assessed continuously. Due to the huge number of DoF, this step is very time-consuming, even if rapid-access models are used. Here, we propose to use model-reduction techniques based on spline as it provides an efficient way to approximate a problem with a large number of DoF. This is classically done to optimize the complex geometry of shaped reflectors [22] and even the geometrical evolution of cells over RA panels [23].

Finally, it is well known [24] that successive cells must not differ too much in their geometry, and a smooth evolution has to be guaranteed all over the RA surface. This is the condition for complying with the local-periodicity assumption. To do so, an additional goal can be added in the optimization process to enforce some kind of similarity between neighbor cells [25]. However, this makes the process even more complex. Moreover, it does not prevent from the abrupt variation encountered after a complete 360° phase cycle has been achieved. A more relevant approach to address this issue is to use Phoenix cell. Thanks to its rebirth property [26], this cell has the unique capability to come back to its initial geometry after a complete 360° cycle has been reached, thus naturally preventing for any abrupt variation. Unfortunately, no RA synthesis has been reported yet, that fully takes benefit of the capabilities of the Phoenix cell. Indeed, most publications involve first order Phoenix cell [27] (i.e., with only one tuning parameter), whose capabilities are of course limited regarding multiple-purpose optimization. On the other hand, higher order Phoenix [6] cell offer additional DoF but the rebirth property is not so easy to handle since the variation domain for the geometry is now multi-dimensional.

The main contribution of this paper is to propose an original spherical mapping of the second order Phoenix cell that intrinsically handles its rebirth mechanism, whatever the variation in the geometrical parameters. This mapping is associated with ANN modeling for a fast characterization of the cell. It is then integrated into an optimization process, which automatically enables to guarantee a smooth evolution of the geometry with no need to use additional constraints. Furthermore, the mapping transforms the initial optimization domain into an unbounded periodic space, and it also reduces its dimension. As a result, we arrive to a quite powerful tool dedicated to the full exploitation of the second order Phoenix cell. This is a first step before addressing the case of higher order cells with even more capabilities.

The paper is organized as follows. Section 2 is dedicated to the presentation of the spherical mapping of the second order Phoenix cell. Section 3 shows its efficient application in RA synthesis. A design example focusing on co-polarization illustrates the good performance for a 83×71 cell RA in section 4 with a full-wave simulation to valid the process. Section 5 concludes the paper.

2. A SPHERICAL MAPPING OF THE 2ND ORDER PHOENIX CELL

The main objective of this section is to present the new spherical mapping of the 2nd order Phoenix cell that will be later used to facilitate the RA synthesis.

2.1. Studied Cell: The 2nd Order Phoenix Cell

Phoenix cells are specific RA cells that have the property to provide a 360° phase range while their geometry evolves in a cycling way, coming back to the initial geometry at the end of the cycle. This so-called rebirth capability theoretically enables designing RA with smooth geometrical variations on the reflecting panel. The concept of Phoenix cells has been proposed originally in [26] and different possible geometries have then been studied such as [28, 29]. A new step has been passed in [27] where two different geometries, one capacitive and the other inductive, are combined successively to form the Phoenix cycle. The main advantage is to provide two complementary phase ranges and hence to avoid any steep resonance, thus preventing for very dispersive behaviors [27]. Figure 1(a) shows a representation of such a typical Phoenix cycle. Here, the capacitive part ($n = 0$) simply consists of a square patch with increasing size (C_1). The inductive part ($n = 1$) is the complementary configuration with the patch replaced by a square aperture. Figure 1(b) gives a wrapped representation of this cycle, clearly showing it provides an unbounded and continuous way of varying the geometry, as a direct consequence of the rebirth property. In the following, we refer to this cycle as a first order one since there is only one geometrical parameter (C_1).

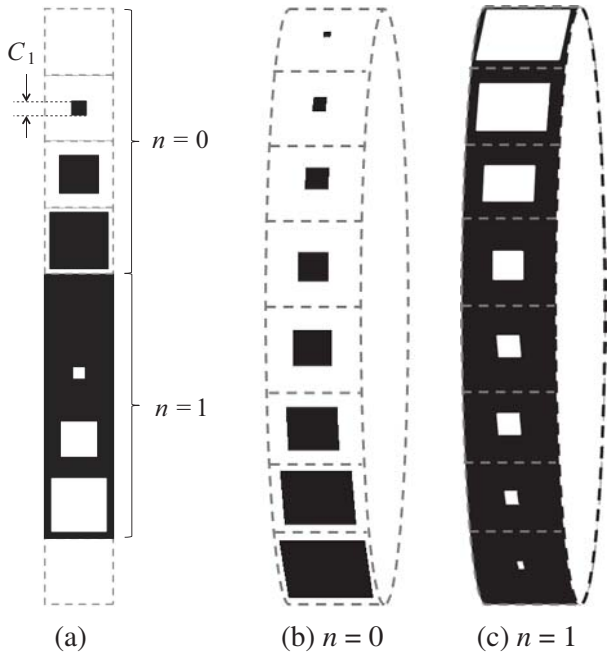

Figure 1. 1D geometrical cycle of the 1st order Phoenix cell. (a) Unwrapped version. Wrapped version — (b) front side and (c) back side.

In this paper, we use the second order of this Phoenix cell by introducing a second geometrical parameter, C_2. To do so, the square patch (or aperture) is replaced by a square ring, as shown in Figure 2. The additional DoF provides more flexibility to control the reflection properties of the cell. On the other hand, it also makes trickier the management of the rebirth capabilities since this one has now to be described in a multi-dimensional space. Indeed, in order to fully benefit from the possibilities offered by the second order Phoenix cell, the representation shown in Figure 1 has to be generalized. This is the objective of the next section.

2.2. Spherical Representation of the 2nd Order Phoenix Cell

The basic rules defining this generalized representation are straightforwardly derived from those observed in Figure 1. Firstly, the representation must include all possible configurations of the cell, whatever its type (n) and its geometrical parameters (C_1 and C_2). Secondly, it must preserve unicity, in the sense that any configuration of the cell is only represented once. Thirdly, it must guarantee a smooth

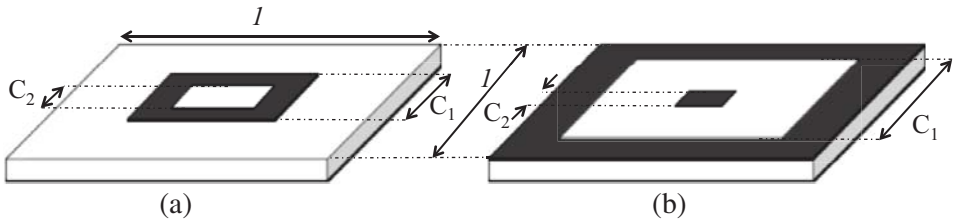

Figure 2. Two different types of cells. (a) Capacitive ($n = 0$). (b) Inductive ($n = 1$).

evolution of the cell geometry all over the representation. Finally, it must not be bounded, i.e., any cell in the representation has to be surrounded by neighbors with slightly-perturbed geometries and none of them should be a stopping boundary.

As seen in Figures 3(a) and (b), a quite natural way to define such a scheme is to use a spherical representation, similar to a world map with a 360° periodicity for θ and ϕ. For the ease of understanding, Figure 3(c) also gives a planisphere version of this representation. The North and South Poles correspond to non-metallized and fully-metallized cells respectively. The 0° and 180° meridians match the capacitive ($n = 0$) and inductive ($n = 1$) parts of first order cycle (Figure 1). They are characterized by $C_2 = 0$. All other cells in the spherical representation are second order cells ($C_2 \neq 0$) also defining continuous cycles in any direction. More precisely, one parallel in the sphere is characterized by cells that all have the same metal rate. This parameter represents the percentage of metal along the length l of the cell. It continuously varies from 0% at the North Pole to 100% at the South Pole.

This representation scheme defines a bijective correspondence between the angular position (θ, ϕ), in degrees, on the sphere and the cell configuration (C_1, C_2, n):

$$\begin{cases} \theta(C_1, C_2, n) = \begin{cases} 180\left(1 - \dfrac{C_2 - C_1 + l}{l}\right) & \text{if } n = 0 \\ \dfrac{180(C_2 - C_1 + l)}{l} & \text{if } n = 1 \end{cases} \\ \phi(C_1, C_2, n) = \begin{cases} \dfrac{180C_2}{C_2 - C_1 + l} & \text{if } n = 0 \\ \dfrac{180C_2}{C_2 - C_1 + l} + 180 & \text{if } n = 1 \end{cases} \end{cases} \tag{1}$$

$$\begin{cases} C_1(\theta, \phi, n) = \begin{cases} \omega(\theta) + (l - \omega(\theta))\dfrac{\phi}{180} & \text{if } n = 0 \\ l - \omega(\theta) + \omega(\theta)\dfrac{(\phi - 180)}{180} & \text{if } n = 1 \end{cases} \\ C_2(\theta, \phi, n) = \begin{cases} (l - \omega(\theta))\dfrac{\phi}{180} & \text{if } n = 0 \\ \omega(\theta)\dfrac{(\phi - 180)}{180} & \text{if } n = 1 \end{cases} \\ \omega(\theta) = \dfrac{l\theta}{180} \end{cases} \tag{2}$$

In these equations, l is the fixed periodicity in the array.

As it will be seen in following sections, this representation proves to be particularly convenient in the RA synthesis process. Indeed, it provides a very powerful tool to deal with the tricky selection of adjacent cells when designing a RA panel. By moving over the sphere, variations in the cell configuration can be achieved with only two tuning parameters (θ and ϕ) in a continuous and periodic domain. Practically, this means the synthesis process can be advantageously carried out by optimizing θ and ϕ instead of dealing with true geometrical parameters. The interest is threefold. Firstly, the number of DoF per cell is reduced from 3 (i.e., C_1, C_2, n) to 2 (i.e., θ and ϕ). Secondly, the structure of the new optimization domain naturally prevents for any abrupt transition in the succession of cells on the panel.

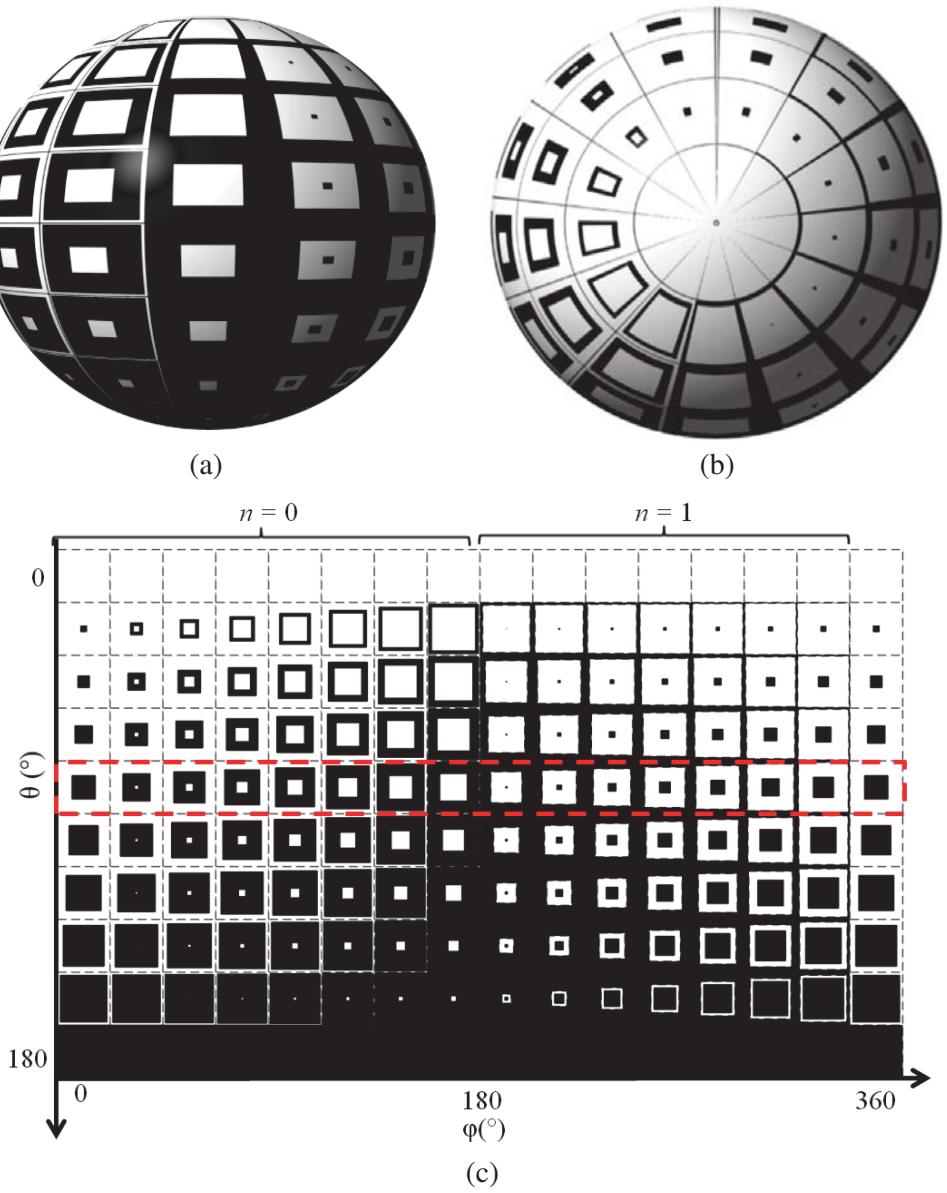

Figure 3. Spherical representation with three overviews. (a) Front side view ($\theta = 90°$, $\phi = 0°$). (b) Top view ($\theta = 0°$ whatever ϕ). (c) Planisphere view.

Thirdly, unconstrained optimization is possible since the new optimization parameters are not bounded as they evolve periodically. Note that the reduction in the number of DoF per cell does not mean the solution space itself is shrunk. It is just organized in a more convenient and compact way that enforces smoothness and continuity over the RA panel. As such, it can be seen as some kind of preconditioning for the optimization process.

2.3. Spherical Mapping of the Main Characteristics

Before going into the details of the synthesis process, we show here that the spherical mapping first offers a very complete and synthetic way to observe the performance of the cell. A cell is classically characterized by its reflection matrix:

$$R = \begin{bmatrix} R_{\text{TE-TE}} & R_{\text{TE-TM}} \\ R_{\text{TM-TE}} & R_{\text{TM-TM}} \end{bmatrix} \tag{3}$$

A rapid-access model is of course required to compute this matrix, whatever the geometry of the cell, the direction of the illuminating wave and the frequency. In this work, we use the ANN model we developed in [19] and [20] to predict both the phase and magnitude for all matrix coefficients. A fast assessment with high accuracy (typically 1.6° RMS error for the phase parameters) was demonstrated compared to full-wave simulation. Combined with the proposed spherical mapping, it enables an overview of the overall performance attainable by the chosen cell. Moreover, as the representation domain naturally guarantees smooth variations in the geometry, it directly shows whether this translates into smooth variations in the matrix coefficients themselves.

As an example, Figure 4 presents the mapping of the $R_{\text{TE-TE}}$ phase calculated using the ANN model over the sphere for all possible cell configurations. The studied cell is printed on a Honeycomb substrate with thickness $h = 20\,\text{mm}$, dielectric constant $\epsilon = 1.03$ and loss tangent $\tan\delta = 0.003$. The periodicity is $l = 25.6\,\text{mm}$ ($\lambda/3$ at 3.9 GHz). The mapping is carried out at normal incidence and for 3 different frequencies. In order to better see the transition in the phase when moving from a capacitive cell to an inductive one (or conversely), the ϕ angle in the planisphere mapping is varied from 0° to 385°. In other words, the $[360°, 385°]$ interval on the right of the plot is a repetition of the $[0°, 25°]$ interval on the left.

The first output from this plot is that any phase value from −180° to 180° can be reached by the cell. Moreover, most of them can be obtained with several different geometries, which provides additional flexibility in the synthesis process. Globally, the plot also shows the phase variations are quite regular. However, one can detect a slight discontinuity (less than 15°) when moving from a capacitive to an inductive cell (at $\phi = 180°$) and a more significant one (up to 50°) when passing the converse transition (at $\phi = 360°$). An optimal trajectory on the sphere would be a closed path passing through all possible phase values while minimizing the discontinuities when n is changed. A closer examination of the plot shows it is achieved by choosing the equator (dotted line in Figure 4(b)). This results from the fact that the discontinuity at the first transition ($\phi = 180°$) gets higher when approaching the South Pole while that at the second transition ($\phi = 360°$) becomes larger close to the North pole. The $R_{\text{TE-TE}}$ phase evolution (at $f = 3.9\,\text{GHz}$) along this equatorial cycle is presented in Figure 5. As we will see later on, this trajectory will play an important role when choosing the initial conditions for the synthesis process.

Finally, the modification of the plot versus frequency is an indicator about dispersion, described in Eq. (4) in °/GHz. A more direct information is given by Figure 6 that plots phase dispersion over the bandwidth. It confirms each phase value can be obtained with various possible dispersion levels. The minimum value, 0°/GHz, is obtained close to the South Pole where the fully-metallized cell is equivalent to a PEC boundary. The maximum value (absolute value), 340°/GHz, is obtained in the back area, where a resonant phenomenon associated with large and narrow slot-rings is encountered.

$$\frac{\Delta\Phi_{\text{TE-TE}}}{\Delta f} = \frac{\Phi_{f_{\max}} - \Phi_{f_{\min}}}{f_{\max} - f_{\min}} \tag{4}$$

3. OPTIMIZATION ALGORITHM

3.1. Goal and Used Cost Function ϵ

In the context of space antennas, the goal of the RA optimization process can be to reach an objective radiated field $\mathbf{E}^{\text{obj}}$ associated with a defined coverage on Earth. This field is specified at N_{sta} station distributed over the Earth and at N_{freq} frequencies f in a given band. To this aim, a min/max optimization process is used [30]. For example, in the case of a co-polar optimization, the cost function is defined as the maximum of the difference between the co-polar components of the objective field and the field $\mathbf{E}^{\text{rad}}$ radiated by the RA under optimization:

$$\epsilon = \max_f \left\{ \max_k \left\{ \left| E_{\text{co}}^{\text{obj}}(k,f) \right| - \left| E_{\text{co}}^{\text{rad}}(k,f) \right| \right\} \right\} \tag{5}$$

with $k = 1, \ldots, N_{\text{sta}}$. In the optimization process, $\mathbf{E}^{\text{rad}}$ is calculated using geometrical optics where the reflection on each cell is obtained from its full scattering matrix (ANN model) with the real incidence angle and far-field illumination from primary horn. The modeled radiation pattern of this horn is derived from measurements.

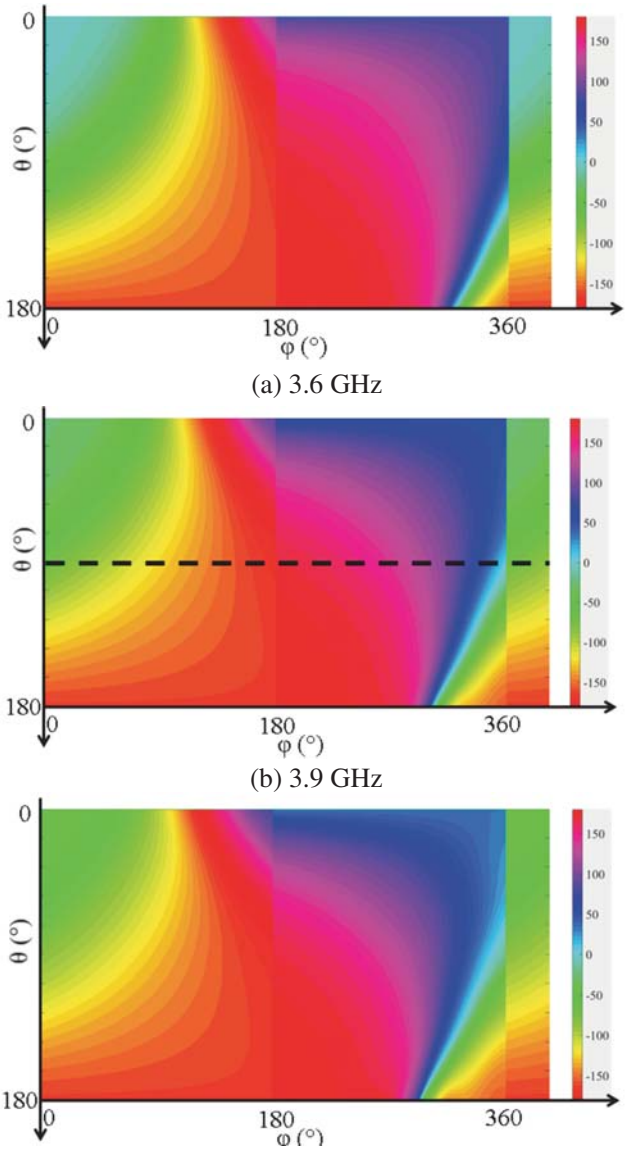

(a) 3.6 GHz

(b) 3.9 GHz

(c) 4.2 GHz

Figure 4. $R_{\text{TE-TE}}$ phase (degrees) on the spherical representation and at different frequencies.

3.2. Optimization DoF and Initial Condition

As already mentioned, we propose to optimize the RA panel directly on the θ and ϕ parameters instead of the true geometrical ones (C_1, C_2, n). For a RA constituted of N^x and N^y cells along x and y axes respectively, the array is entirely defined by θ_{ij} and ϕ_{ij} for $i \in [1, N^x]$ and $j \in [1, N^y]$. The initial number of DoF is thus given by:

$$N_{\text{DoF}_{\text{init}}} = 2N^x N^y \tag{6}$$

Classically, the optimizer starts from an initial condition defined by θ^0_{ij} and ϕ^0_{ij}. To derive this one, the equator cycle discussed in Section 2.3 is used. It provides a one-to-one correspondence between cell geometry and local phase while minimizing the phase discontinuities along the cycle. The initial layout is built by only satisfying the required co-polarization phase over the panel (accounting for local field incidence) and at the central frequency with classical Phase Only Synthesis techniques [31, 32]. However, there is no reason for it to work properly for other frequencies and for the cross-polarization. Accordingly, the RA panel performance must be optimized.

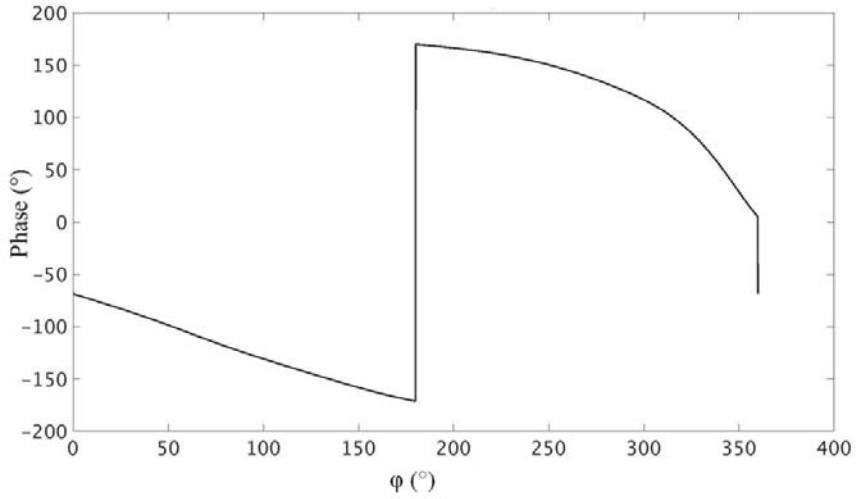

Figure 5. $R_{\text{TE-TE}}$ phase evolution along the equatorial cycle at the central frequency 3.9 GHz.

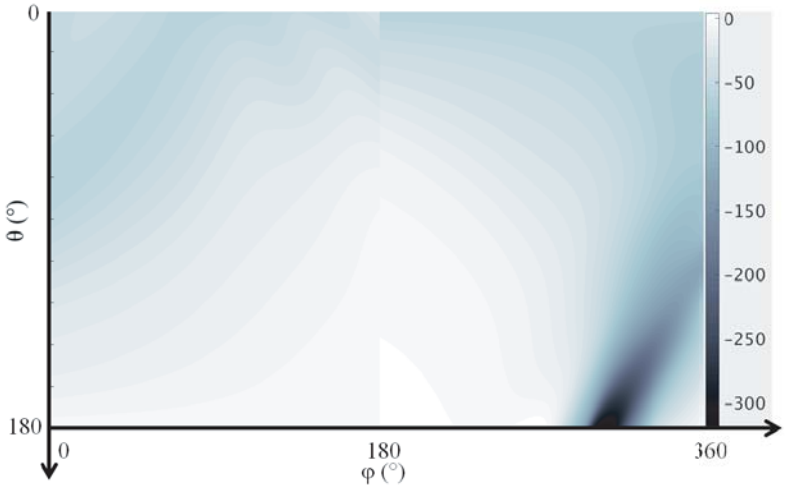

Figure 6. Dispersion over the bandwidth of the $R_{\text{TE-TE}}$ phase (degrees/GHz) on the spherical representation and at the central frequency 3.9 GHz.

To vary θ_{ij} and ϕ_{ij} from the initial layout within the optimization process, $\Delta\theta_{ij}$ and $\Delta\phi_{ij}$ are introduced:

$$\begin{cases} \theta_{ij} = \theta_{ij}^{0} + \Delta\theta_{ij} \\ \phi_{ij} = \phi_{ij}^{0} + \Delta\phi_{ij} \end{cases} \tag{7}$$

$\Delta\theta_{ij}$ and $\Delta\phi_{ij}$ are the new $N_{\text{DoF}_{\text{init}}}$ parameters to be optimized. For space applications, $N_{\text{DoF}_{\text{init}}}$ can be huge reaching up to several thousands. For computation time and convergence reasons, the complexity is reduced by expanding the unknowns on approximation functions so that the required information is compressed without sacrificing accuracy:

$$\begin{cases} \Delta\theta_{ij} = \displaystyle\sum_{l=1}^{N_{Sx}} c_l^x S_l^x(x_i) \sum_{m=1}^{N_{Sy}} c_m^y S_m^y(y_j) \\ \Delta\phi_{ij} = \displaystyle\sum_{l=1}^{N_{Sx}} d_l^x S_l^x(x_i) \sum_{m=1}^{N_{Sy}} d_m^y S_m^y(y_j) \end{cases} \tag{8}$$

In this equation, S_l^x and S_m^y are bi-cubic spline basis functions [33] along x and y respectively, N_{S^x} and N_{S^y} are the numbers of these functions, x_i and y_j are the center coordinates of the (i, j) cell and $c_{l/m}^{x/y}$ and $d_{l/m}^{x/y}$ are the spline expansion coefficients. This approach is largely inspired by the techniques used to optimize shaped reflectors for space applications [22] and has also been used for RA [23]. The main issue consists in choosing the appropriate number of expansion functions so that the approximation is precise enough. Furthermore, the choice of the resolution also enables controlling the smoothness of geometrical variations over the panel. In practise, it may be increased gradually until a sufficient accuracy is reached, as it is classically done when designing shaped reflectors. Finally, the number of optimization DoF N_{DoF} is compressed to:

$$N_{\mathrm{DoF}} = 2N_{S^x}N_{S^y} \tag{9}$$

Strictly speaking, this is not really a reduction in the number of available DoF but a compressed representation of them.

3.3. Optimization Algorithm

Based on the min/max algorithm, the objective is to minimize the cost function (Eq. (5)) by modifying the spline coefficients. To achieve this, an off-the-shelf conventional iterative gradient descent is used. In order to get the best orientation in the DoF space, the following gradient vector G is calculated numerically at each iteration:

$$G = \left[\frac{\partial\epsilon}{\partial c_1^x}\cdots\frac{\partial\epsilon}{\partial c_{N_{S^x}}^x}\ \frac{\partial\epsilon}{\partial c_1^y}\cdots\frac{\partial\epsilon}{\partial c_{N_{S^y}}^y}\frac{\partial\epsilon}{\partial d_1^x}\cdots\frac{\partial\epsilon}{\partial d_{N_{S^x}}^x}\ \frac{\partial\epsilon}{\partial d_1^y}\cdots\frac{\partial\epsilon}{\partial d_{N_{S^y}}^y}\right] \tag{10}$$

Figure 7 summarizes the algorithm.

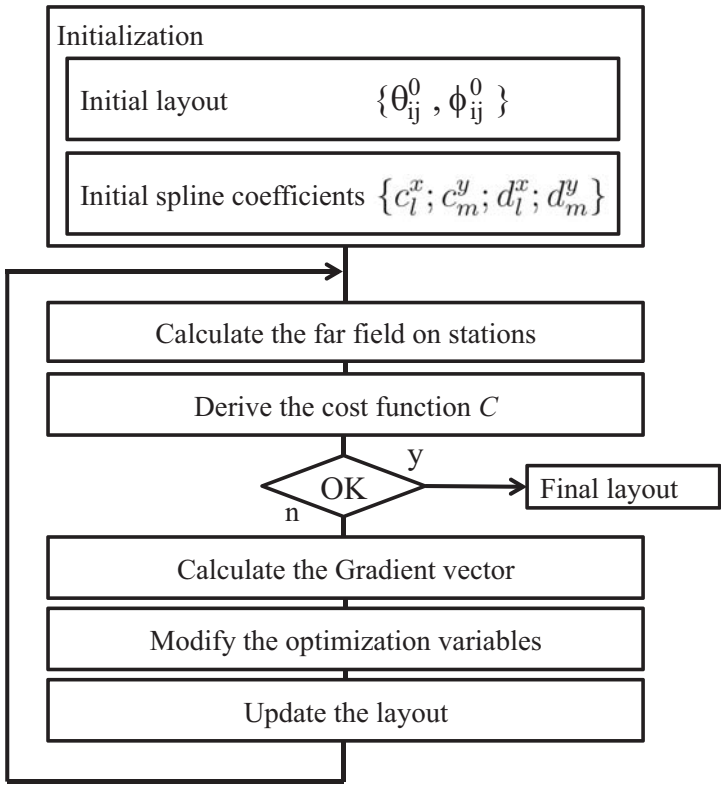

Figure 7. General optimization algorithm.

4. APPLICATION TO A C-BAND MISSION

4.1. Mission Specifications

To illustrate the algorithm performances, we consider a C-band space telecommunication mission. The coverage zones are shown in Figure 8 and the co-polarization (co-polar) gain and cross-polarization discrimination (XPD) requirements are summarized in Table 1. The purpose of the mission is to provide service to Europe, North Africa and Middle East (FC1 zone) while minimizing illumination in South America (FC2 zone). The antenna operates in left-handed circular polarization in the limited transmission C-band $[3.6, 4.2]$ GHz.

Table 1. Coverage requirements.

Zone	Co-polar Gain_{min} [dB]	Co-polar Gain_{max} [dB]	XPD_{min} [dB]
FC1	24.2	X	28.0
FC2	X	10.0	X

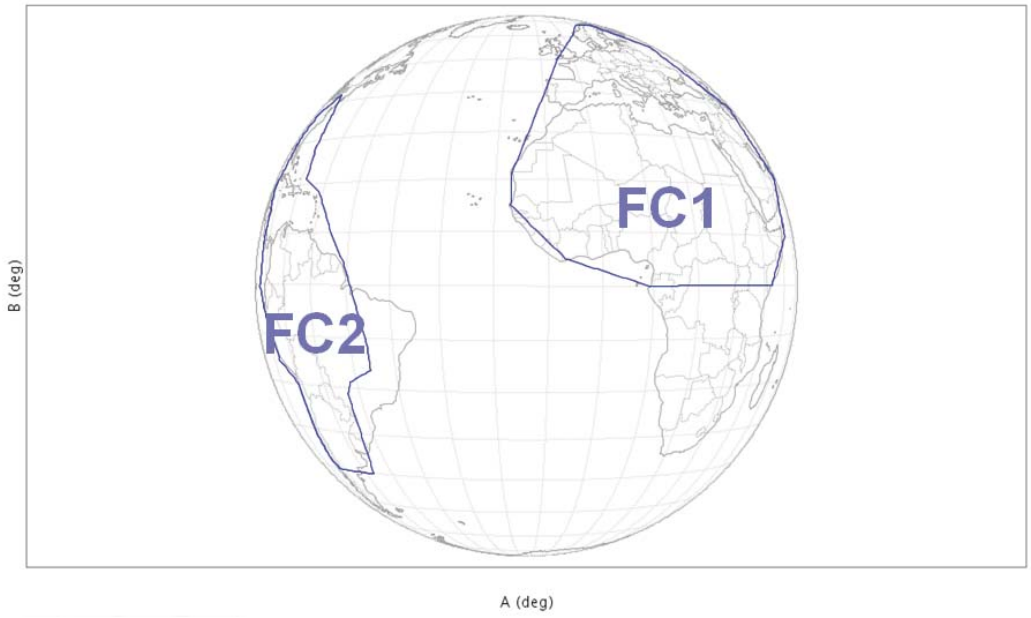

Figure 8. Coverage zones of the telecommunication mission. FC1: co-polar directivity. FC2: co-polar isolation.

4.2. Antenna and Optimization Parameters

This work concerns only the layout design, and the antenna system parameters such as the feeding antenna type and position and the RA dimensions are fixed and given in Figure 9.

The RA panel is 28λ along x and 24λ along y at the central frequency $f = 3.9\,\text{GHz}$. The array periodicity is $\lambda/3$ along x and y resulting in $N^x = 83$ and $N^y = 71$ RA cells, the initial number of optimization DoF is thus $N_{\text{DoF}_{\text{init}}} = 11786$.

In order to drastically compress the information and insure smooth geometrical variations around the initial condition, the numbers of spline coefficients N_{S^x} and N_{S^y} are both chosen to 20. The final

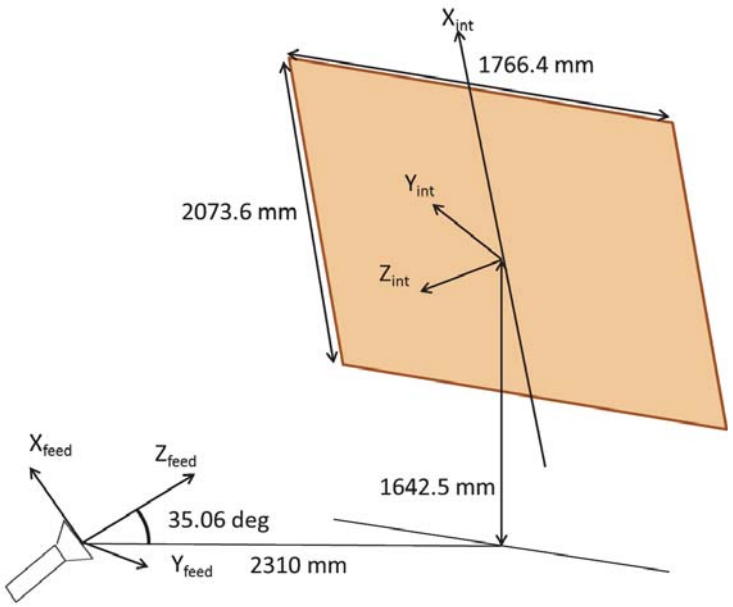

Figure 9. Fixed antenna architecture.

number of optimization DoF is then $N_{\mathrm{DoF}} = 800$. N_{sta} is set to 300 station points with a uniform distribution in the zone of interest.

In this paper, the developed mapping is restricted to the 2nd order cell. Such a cell intrinsically offers no simple means of controlling cross-polar because it has a square symmetric geometry. Then in this example, we decided to focus only on co-polarization and try to optimize it on a quite large bandwidth (16%). Consequently, no goal was given for the cross.

Introducing new geometrical parameters, XPD could be optimized as it is done in [34] by converting square Phoenix cells into rectangular ones or by the use of parallelogram or trapezoid shaped elements as in [31]. Cross-polarization could also theoretically be optimized at the array level with symmetrical cells [35]. Once again, this was not possible here as all available DoF were already necessary to address the co-polar specifications (for both the illuminated and isolated zones) over the bandwidth.

4.3. Initial Layout

The required co-polarization phase distribution on the RA at the central frequency $f = 3.9\,\mathrm{GHz}$ is presented in Figure 10. Using the equator cycle and its one-to-one correspondence between cell geometry and reflected co-polar phase, the initial layout is easily designed. As shown in Figure 11, this layout presents smooth geometrical variations. This property tends to respect the expected local periodicity for the cells.

The simulated radiation patterns of the initial layout are presented in Figure 12(a), and the achieved performances are synthesized in Table 2. As expected, the performances respect the specifications only at the central frequency $f = 3.9\,\mathrm{GHz}$ and for the radiated co-polar.

4.4. Optimization Run

Figure 13 presents the evolution of the cost function with iterations. Clearly, the optimization converges since the cost function decreases with the iteration number and tends to zero. The optimization was carried out using a workstation with a 2.5-GHz dual-core AMD Opteron processor with 128 GB RAM. The computation time is around 12 hours. Note that the simulation time for one cell is 4 µs using ANN. It would be around 1 min for full-wave simulation, which is definitely intractable within an optimization process. The total computation time could be reduced further by improving the present min/max routine and the radiation pattern calculation (to be done several times at each iteration in order to

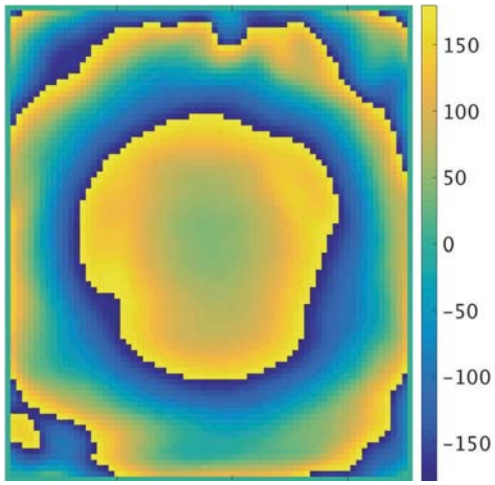

Figure 10. Ideal $R_{TE\text{-}TE}$ phase (degrees) requirement at 3.9 GHz.

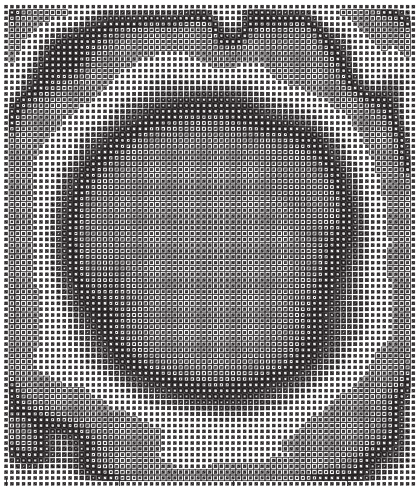

Figure 11. Initial layout for the C-band mission.

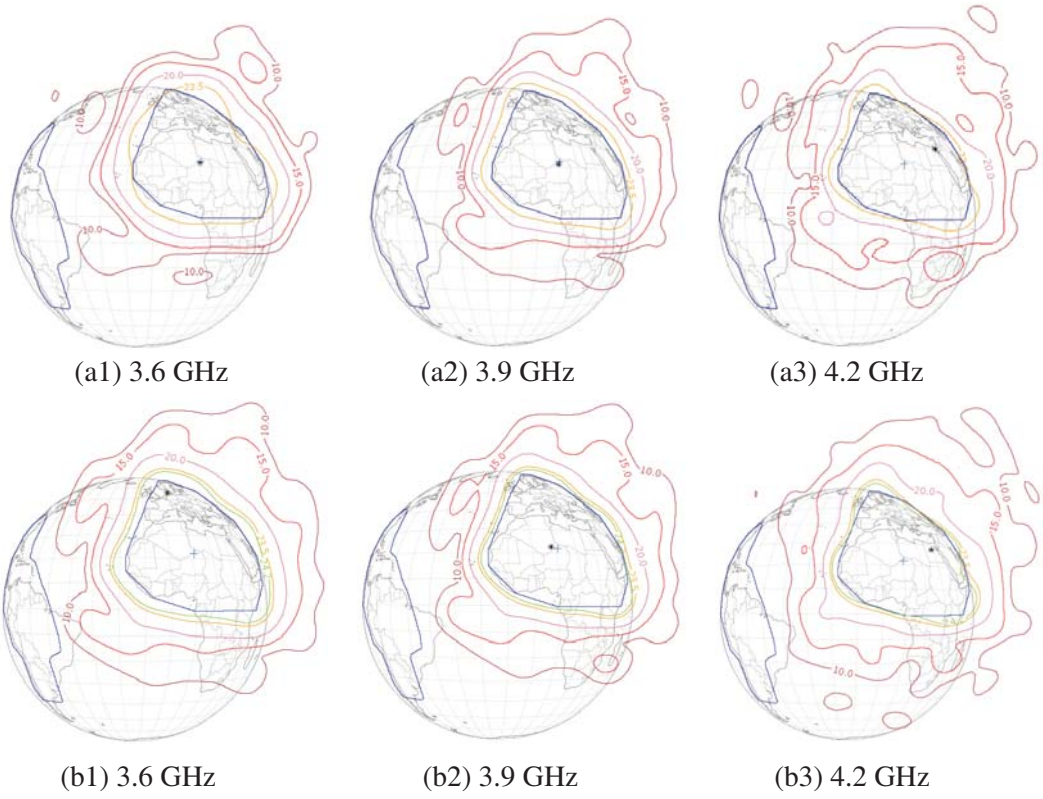

Figure 12. Simulated radiation pattern in co-polarization gain [dBi] for left polarization at different frequencies. (a) Initial RA. (b) Optimized RA.

calculate gradients given by Eq. (10)). Such improvements were not addressed in this study, whose main scope was the spherical mapping.

Figure 12(b) presents the radiation patterns of the optimized RA. Compared to the initial RA ones, we clearly observe the benefits of the optimization process at the lateral frequencies. Table 3 confirms this observation since the co-polar gain specifications are now reached at 3.6 GHz and 3.9 GHz. Only a small 0.06 dBi residual error is noted at 4.2 GHz. Note that the gain improvement compared to an

Table 2. Initial RA performances.

Frequency GHz	Zone	Co-polar $Gain_{min}$ [dB]	Co-polar $Gain_{max}$ [dB]	XPD_{min} [dB]
3.6	FC1	23.03	X	21.6
	FC2	X	9.52	X
3.9	FC1	24.36	X	22.47
	FC2	X	6.7	X
4.2	FC1	22.7	X	21.95
	FC2	X	7.84	X

Table 3. Optimized RA performances.

Frequency GHz	Zone	Co-polar $Gain_{min}$ [dB]	Co-polar $Gain_{max}$ [dB]	XPD_{min} [dB]
3.6	FC1	24.65	X	22.52
	FC2	X	7.62	X
3.9	FC1	24.28	X	22.09
	FC2	X	6.46	X
4.2	FC1	24.14	X	20.25
	FC2	X	7.43	X

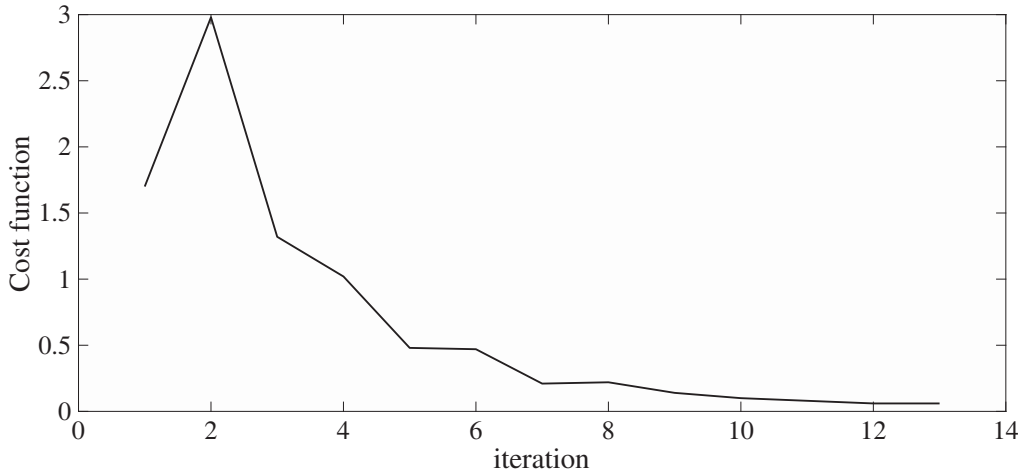

Figure 13. Convergence of the cost function.

initial POS is up to 1.62 dB. Concerning the XPD, the specifications are obviously not reached since it has not been considered in the cost function. However, the XPD has not been too much affected by the co-polar optimization process.

4.5. Validation by Full-Wave Simulation

For validation purpose, a full-wave simulation of the whole antenna system is proposed in this section. A homemade solver based on integral equations in frequency domain is used [36]. Figure 14 shows the comparison between the full-wave solver results and the one obtained with array theory under local periodicity assumption.

It must be highlighted that the agreement is very good. This definitely shows that the reached geometrical continuity over the panel is a key point to comply with the local periodicity assumption. Thanks to that, conventional array theory can be used with confidence in the optimizing process.

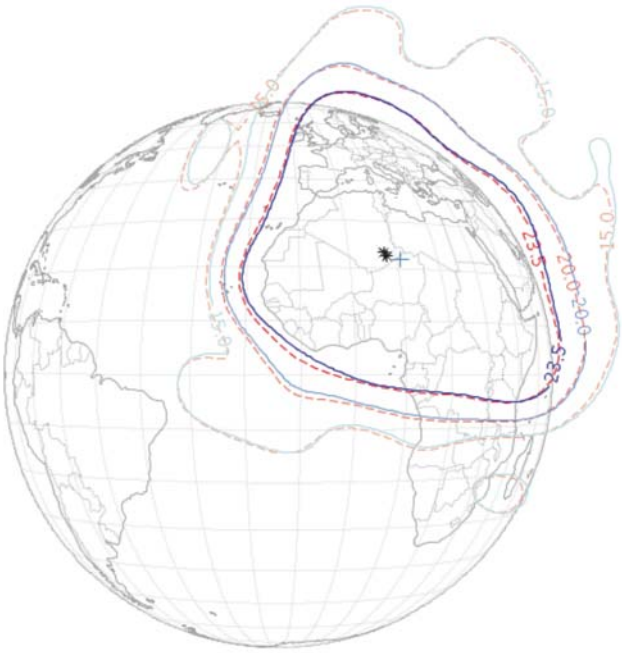

Figure 14. Comparison of radiation patterns obtained with full-wave solver (blue curves) and homemade analytical tool (red curves) at 3.9 GHz.

5. CONCLUSION

This paper describes an original spherical mapping for the 2nd order Phoenix cell. It appears as an essential tool to fully benefit from this versatile but complex cell. It first provides a convenient way to visualize its overall properties. Moreover, it leads to an optimization domain that directly inherits its continuous and cyclic evolution. This makes it fully suitable with spline that leads to a compressed formulation of the problem to be optimized. In this paper, the mapping is combined with ANN modeling and encapsulated in a min/max optimization process, thus resulting in a general optimization package. It is successfully applied to optimize a contoured beam coverage for space communication on a 16% frequency bandwidth. The gain at the upper frequency is improved by 1.62 dB compared to the initial POS. The excellent agreement with full-wave simulation confirms that the proposed methodology automatically generates a regular RA layout that naturally complies with the implicit local-periodicity assumption.

Further work is now needed to extend the mapping to higher order or asymmetrical cells, which will offer additional DoF, especially for the management of the cross-polarization.

REFERENCES

1. Huang, J. and J. A. Encinar, *Reflectarray Antennas*, Wiley-IEEE Press, Nov. 2007, ISBN: 978-0-470-08491-5.
2. Encinar, J. A., "Design of two-layer printed reflectarrays using patches of variable size," *IEEE Transactions on Antennas and Propagation*, Vol. 49, No. 10, 1403–1410, Oct. 2001.
3. Karimipour, M., A. Pirhadi, and N. Ebrahimi, "Accurate method for synthesis of shaped-beam non-uniform reflectarray antenna," *IET Microwaves, Antennas and Propagation*, Vol. 7, No. 15, 1247–1253, Dec. 2013.
4. Encinar, J. A. and J. A. Zornoza, "Three-layer printed reflectarrays for contoured beam space applications," *IEEE Transactions on Antennas and Propagation*, Vol. 52, No. 5, 1138–1148, May 2004.
5. Zhou, M., S. B. Sorensen, R. Jorgensen, O. Borries, E. Jorgensen, and G. Toso, "High-performance curved contoured beam reflectarrays with reusable surface for multiple coverages," *2017 11th European Conference on Antennas and Propagation (EUCAP)*, 71–75, Mar. 2017.
6. Legay, H., D. Bresciani, E. Labiole, R. Chiniard, R. Gillard, and G. Toso, "Measurement of a 1.3 m reflectarray antenna in at panels in ku band," *2012 International Symposium on Antennas and Propagation (ISAP)*, 231–234, Oct. 2012.
7. Hasani, H., C. Peixeiro, A. K. Skrivervik, and J. Perruisseau-Carrier, "Single-layer quad-band printed reflectarray antenna with dual linear polarization," *IEEE Transactions on Antennas and Propagation*, Vol. 63, No. 12, 5522–5528, Dec. 2015.
8. Florencio, R., J. A. Encinar, R. R. Boix, V. Losada, and G. Toso, "Reflectarray antennas for dual polarization and broadband telecom satellite applications," *IEEE Transactions on Antennas and Propagation*, Vol. 63, No. 4, 1234–1246, Apr. 2015.
9. Bucci, O. M., A. Capozzoli, G. D'Elia, and S. Musto, "A new approach to the power pattern synthesis of reflectarrays," *Proc. URSI International Symposium on Electromagnetic Theory (EMTS'04)*, 1053–1055, 2004.
10. Zhou, M., S. B. Srensen, O. S. Kim, E. Jrgensen, P. Meincke, and O. Breinbjerg, "Direct optimization of printed reflectarrays for contoured beam satellite antenna applications," *IEEE Transactions on Antennas and Propagation*, Vol. 61, No. 4, 1995–2004, Apr. 2013.
11. Wan, C. and J. A. Encinar, "Efficient computation of generalized scattering matrix for analyzing multilayered periodic structures," *IEEE Transactions on Antennas and Propagation*, Vol. 43, No. 11, 1233–1242, Nov. 1995.
12. Al-Joumayly, M. A. and N. Behdad, "A generalized method for synthesizing low-profile, band-pass frequency selective surfaces with non resonant constituting elements," *Int. Journal of Antennas and Propag.*, Vol. 58, No. 12, 4033–4041, Dec. 2010.
13. Liang, L. and S. V. Hum, "An impedance surface-based method for designing wideband reflectarrays," *2015 IEEE Int. Sym. on Ant. and Propag. USNC/URSI Nat. Radio Science Meeting*, 2135–2136, Jul. 2015.
14. Zhou, M., S. B. Sorensen, N. Vesterdal, R. Dickie, P. Baine, J. Montgomery, R. Cahill, M. Henry, P. G. Huggard, and G. Toso, "Design of aperiodic frequency selective surfaces for compact quasioptical networks," *2017 11th European Conference on Antennas and Propagation (EUCAP)*, 1274–1278, Mar. 2017.
15. Hum, S. V. and B. Du, "Equivalent circuit modeling for reflectarrays using oquet modal expansion," *IEEE Transactions on Antennas and Propagation*, Vol. 65, No. 3, 1131–1140, Mar. 2017.
16. Robustillo, P., J. Zapata, J. A. Encinar, and J. Rubio, "Ann characterization of multi-layer reflectarray elements for contoured-beam space antennas in the ku-band," *IEEE Transactions on Antennas and Propagation*, Vol. 60, No. 7, 3205–3214, Jul. 2012.
17. Freni, A., M. Mussetta, and P. Pirinoli, "Neural network characterization of reflectarray antennas," *Int. Journal of Antennas and Propag.*, Vol. 2012, Article ID 541354, 10 pages, May 2012.

18. Robustillo, P., J. Zapata, J. A. Encinar, and M. Arrebola, "Design of a contoured-beam reflectarray for a eutelsat european coverage using a stacked-patch element characterized by an artificial neural network," *IEEE Antennas and Wireless Propagation Letters*, Vol. 11, 977–980, 2012.
19. Richard, V., R. Loison, R. Gillard, H. Legay, and M. Romier, "Optimized artificial neural network for reflectarray cell modelling," *2016 IEEE International Symposium on Antennas and Propagation (APSURSI)*, 1211–1212, Jun. 2016.
20. Richard, V., R. Loison, R. Gillard, H. Legay, and M. Romier, "Loss analysis of a reflectarray cell using anns with accurate magnitude prediction," *2017 11th European Conference on Antennas and Propagation (EUCAP)*, 2396–2399, Mar. 2017.
21. Salucci, M., L. Tenuti, G. Oliveri, and A. Massa, "Efficient prediction of the em response of reflectarray antenna elements by an advanced statistical learning method," *IEEE Transactions on Antennas and Propagation*, Vol. 66, No. 8, 3995–4007, Aug. 2018.
22. Engineering Consultants, POS, *User's Manual*, TICRA, 2001.
23. Zhou, M., S. B. Srensen, E. Jrgensen, and P. Meincke, "Efficient optimization of large reflectarrays using continuous functions," *2013 7th European Conference on Antennas and Propagation (EuCAP)*, 2952–2956, Apr. 2013.
24. Milon, M. A., R. Gillard, D. Cadoret, and H. Legay, "Analysis of mutual coupling for the simulation of reflectarrays radiating cells," *2006 First European Conference on Antennas and Propagation*, 1–6, Nov. 2006.
25. Marnat, L., R. Loison, R. Gillard, D. Bresciani, and H. Legay, "Comparison of synthesis strategies for a dual-polarized reflectarray," *Int. Journal of Antennas and Propag.*, Vol. 2012, Article ID 708429, 10 pages, 2012.
26. Moustafa, L., R. Gillard, F. Peris, R. Loison, H. Legay, and E. Girard, "The Phoenix cell: A new reflectarray cell with large bandwidth and rebirth capabilities," *IEEE Antennas and Wireless Propagation Letters*, Vol. 10, 71–74, 2011.
27. Makdissy, T., R. Gillard, E. Fourn, M. Ferrando-Rocher, E. Girard, H. Legay, and L. Le Coq, "Phoenix: Reflectarray unit cell with reduced size and inductive loading," *IET Microwaves Antennas Propagation*, Vol. 10, 1363–1370, 2016.
28. Salti, H. and R. Gillard, "A single layer stub-patch phoenix cell for large band reflectarrays," *2017 11th European Conf. on Ant. and Propag.*, 2405–2408, Mar. 2017.
29. Zhang, K., Y. Fan, J. Xu, and C. Qu, "Design of broadband, low cost single layer reflectarray using phoenix cell," *2013 IEEE International Conference of IEEE Region 10 (TENCON 2013)*, 1–4, Oct. 2013.
30. Hald, J. and K. Madsen, "Combined lp and quasi newton methods for minimax optimization," *Math. Programming*, Vol. 20, 49–62, 1981.
31. Legay, H., D. Bresciani, E. Labiole, R. Chiniard, and R. Gillard, "A multi facets composite panel reflectarray antenna for a space contoured beam antenna in ku band," *Progress In Electromagnetics Research*, Vol. 54, 1–26, 2013.
32. Encinar, J. A., M. Arrebola, L. F. de la Fuente, and G. Toso, "A transmit-receive reflectarray antenna for direct broadcast satellite applications," *IEEE Transactions on Antennas and Propagation*, Vol. 59, No. 9, 3255–3264, Sept. 2011.
33. De Boor, C., *A Practical Guide to Splines*, Vol. 27, Springer-Verlag New York, 1978.
34. Zhou, M., O. Borries, and E. Jrgensen, "Design and optimization of a single-layer planar transmitreceive contoured beam reflectarray with enhanced performance," *IEEE Transactions on Antennas and Propagation*, Vol. 63, No. 4, 1247–1254, Apr. 2015.
35. Encinar, J. A. and M. Arrebola, "Reduction of cross-polarization in contoured beam reflectarrays using a three-layer configuration," *2007 IEEE Antennas and Propagation Society International Symposium*, 5303–5306, IEEE, 2007.
36. Martinaud, J. P., S. Nosal, and G. Salin, "Domain decomposition techniques for the scattering by partly bor objects application to the antenna-radome modeling," *2011 International Conference on Electromagnetics in Advanced Applications*, 144–147, Sep. 2011.